

## Article

# Numerical Investigation and Device Architecture Optimization of Sb<sub>2</sub>Se<sub>3</sub> Thin-Film Solar Cells Using SCAPS-1D

Chung-Kuan Lai  and Yi-Cheng Lin \* 

Department of Mechatronics Engineering, National Changhua University of Education, Changhua 50007, Taiwan; cklai0703@gmail.com

\* Correspondence: ielinyc@cc.ncue.edu.tw

**Abstract:** Antimony selenide (Sb<sub>2</sub>Se<sub>3</sub>) shows promise for photovoltaics due to its favorable properties and low toxicity. However, current Sb<sub>2</sub>Se<sub>3</sub> solar cells exhibit efficiencies significantly below their theoretical limits, primarily due to interface recombination and non-optimal device architectures. This study presents a comprehensive numerical investigation of Sb<sub>2</sub>Se<sub>3</sub> thin-film solar cells using SCAPS-1D simulation software, focusing on device architecture optimization and interface engineering. We systematically analyzed device configurations (substrate and superstrate), hole-transport layer (HTL) materials (including NiO<sub>x</sub>, CZTS, Cu<sub>2</sub>O, CuO, CuI, CuSCN, CZ-TA, and Spiro-OMeTAD), layer thicknesses, carrier densities, and resistance effects. The substrate configuration with molybdenum back contact demonstrated superior performance compared with the superstrate design, primarily due to favorable energy band alignment at the Mo/Sb<sub>2</sub>Se<sub>3</sub> interface. Among the investigated HTL materials, Cu<sub>2</sub>O exhibited optimal performance with minimal valence-band offset, achieving maximum efficiency at 0.06 μm thickness. Device optimization revealed critical parameters: series resistance should be minimized to 0–5 Ω·cm<sup>2</sup> while maintaining shunt resistance above 2000 Ω·cm<sup>2</sup>. The optimized Mo/Cu<sub>2</sub>O(0.06 μm)/Sb<sub>2</sub>Se<sub>3</sub>/CdS/i-ZnO/ITO/Al structure achieved a remarkable power conversion efficiency (PCE) of 21.68%, representing a significant improvement from 14.23% in conventional cells without HTL. This study provides crucial insights for the practical development of high-efficiency Sb<sub>2</sub>Se<sub>3</sub> solar cells, demonstrating the significant impact of device architecture optimization and interface engineering on overall performance.



**Citation:** Lai, C.-K.; Lin, Y.-C. Numerical Investigation and Device Architecture Optimization of Sb<sub>2</sub>Se<sub>3</sub> Thin-Film Solar Cells Using SCAPS-1D. *Materials* **2024**, *17*, 6203. <https://doi.org/10.3390/ma17246203>

Academic Editor: Artur Chrobak

Received: 26 November 2024

Revised: 8 December 2024

Accepted: 15 December 2024

Published: 19 December 2024



**Copyright:** © 2024 by the authors. Licensee MDPI, Basel, Switzerland. This article is an open access article distributed under the terms and conditions of the Creative Commons Attribution (CC BY) license (<https://creativecommons.org/licenses/by/4.0/>).

**Keywords:** Sb<sub>2</sub>Se<sub>3</sub> solar cells; hole-transport layer; SCAPS-1D; shallow acceptor density; series and shunt resistance

## 1. Introduction

Antimony selenide (Sb<sub>2</sub>Se<sub>3</sub>) represents a promising advancement in photovoltaic technology, characterized by its unique one-dimensional crystal structure and tunable direct bandgap (1.2–1.9 eV) [1]. This material system offers multiple advantages for solar-cell applications, including exceptional photoelectric properties, high absorption coefficient, minimal environmental impact, and cost-effectiveness due to earth-abundant constituents [2]. However, Sb<sub>2</sub>Se<sub>3</sub> solar cells face significant performance limitations, primarily due to reduced open-circuit voltage resulting from carrier recombination at metal back contact interfaces and performance degradation caused by surface oxidation [3]. Various strategies have been implemented to enhance Sb<sub>2</sub>Se<sub>3</sub> solar-cell performance, including doping mechanisms, defect engineering, and interface optimization [4,5]. Notable advances include tellurium doping for defect passivation and transition metal oxide implementation (NiO<sub>x</sub>, MoO<sub>x</sub>) for band alignment optimization. Recent developments, such as the solvent-assisted hydrothermal deposition (SHD) technique, have achieved efficiency improvements of up to 10.75% [6]. Nevertheless, these efficiencies remain significantly below the theoretical Shockley–Queisser (S-Q) limit and the performance of conventional thin-film photovoltaics.

The HTL plays a crucial role in thin-film solar cells by facilitating efficient hole transport while blocking electrons, thereby preventing charge recombination. Additionally, it

optimizes energy-level alignment between the active layer and electrode while enhancing interface quality, ultimately improving PCE [7]. Contemporary research encompasses various HTL materials, including NiO<sub>x</sub> [8,9], CZTS [10,11], CuI [12], Cu<sub>x</sub>O [13,14], CuSCN [15,16], CZ-TA [17,18], AgInTe<sub>2</sub> [19], MoSe<sub>2</sub> [20,21], and Spiro-OMeTAD [22–24]. While experimental studies dominate the field, comprehensive numerical investigations incorporating device structure optimization with HTL material selection remain limited. Among available solar-cell simulation tools, including AMPS1D and wxAMPS-1D [25–27], SCAPS-1D [12,17,19,28–30] has emerged as the preferred platform for Sb<sub>2</sub>Se<sub>3</sub> solar-cell research. This study employed SCAPS-1D software (version 3.3.11) to conduct comprehensive numerical simulation and performance optimization of Sb<sub>2</sub>Se<sub>3</sub> thin-film solar cells. The investigation encompassed device structures (substrate and superstrate configurations), HTL material optimization, thickness effects, shallow acceptor densities, and the impact of series and shunt resistance parameters. The aim of these simulations was to accelerate theoretical understanding and facilitate performance breakthroughs in Sb<sub>2</sub>Se<sub>3</sub> solar-cell technology.

## 2. Device Structure and Simulation Parameters

### 2.1. Device Structure

Solar-cell device structures can be classified into two main categories: substrate and superstrate configurations. Figure 1a, with CdS positioned below the absorber layer, represents the substrate configuration [31], while Figure 1b, with CdS located above the absorber layer, illustrates the superstrate configuration. This investigation systematically examines three distinct device architectures: substrate and superstrate configurations without HTLs (Figures 1a and 1b, respectively), followed by an advanced architecture incorporating an HTL (Figure 1c). In these solar-cell structures, molybdenum (Mo), fluorine-doped tin oxide (FTO), and aluminum (Al) serve as electron-collecting front contacts and hole-collecting back contacts. Antimony selenide (Sb<sub>2</sub>Se<sub>3</sub>) functions as the primary absorber layer, while cadmium sulfide (CdS) serves as the wide-bandgap window layer. Adjacent to the buffer layer, a highly resistive intrinsic zinc oxide (i-ZnO) layer is implemented, overlaid with tin-doped indium oxide (ITO) functioning as a transparent conductive oxide (TCO) to facilitate efficient charge collection and transport through the device. Additionally, i-ZnO acts as a buffer layer between CdS and ITO layers, while its undoped nature reduces interface recombination. It aids in band alignment for efficient charge transport and protects underlying layers during ITO deposition.

### 2.2. Numerical Method

The analysis of SCAPS-1D (version 3.3.11) is based upon Poisson's equation, hole continuity, and electron continuity, as given below [29]:

$$\frac{\partial^2 \varphi}{\partial x^2} + \frac{q}{\varepsilon} [p(x) - n(x) + N_D - N_A + \rho_p - \rho_n] = 0 \quad (1)$$

$$\frac{1}{q} \frac{dJ_p}{dx} = G_{op}(x) - R(x) \quad (2)$$

$$\frac{1}{q} \frac{dJ_n}{dx} = -G_{op}(x) - R(x) \quad (3)$$

where  $\varepsilon$  is the dielectric constant;  $q$  is the electron charge;  $N_A$  and  $N_D$  are acceptor and donor type density, respectively;  $\varphi$  is the electrostatic potential; and  $p$ ,  $n$ ,  $\rho_p$ ,  $\rho_n$ ,  $J_p$ , and  $J_n$  are hole concentration, electron concentration, hole distribution, electron distribution, current densities of holes, and current densities of electrons, respectively.  $G_{op}$  is the optical generation rate, and  $R$  is the net recombination from direct and indirect recombination. All of these parameters are the function of the position coordinate  $x$ .

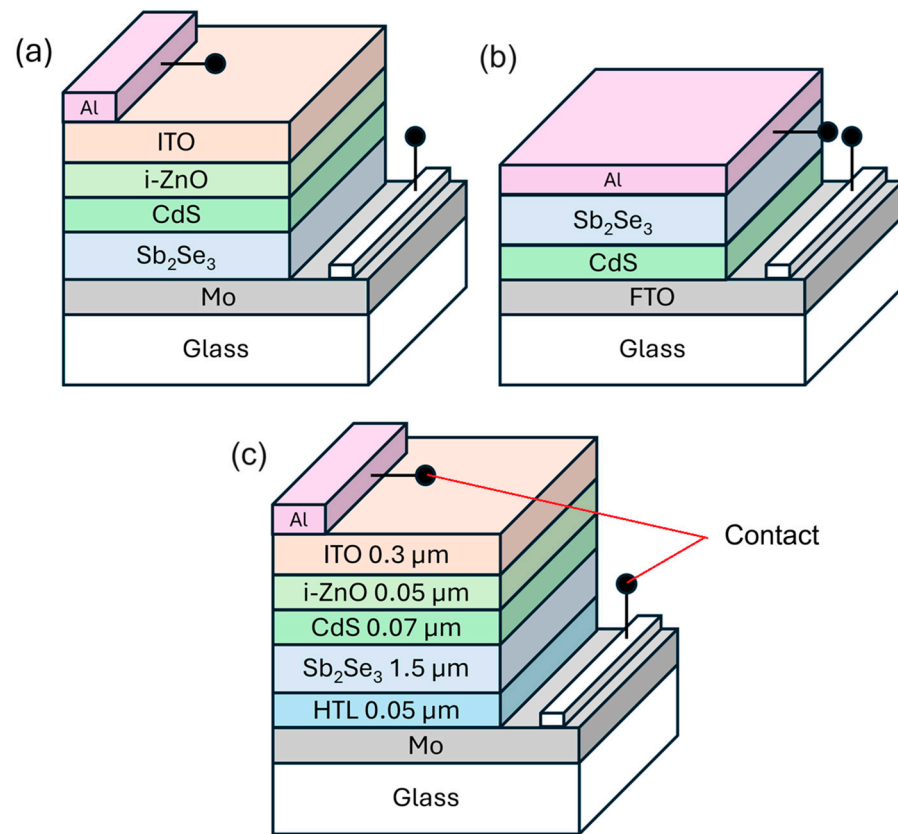


**Figure 1.** Schematic diagram of the proposed solar-cell structure: (a) p-n substrate configuration, (b) p-n superstrate configuration, (c) n-p-p<sup>+</sup> substrate configuration.

The numerical simulation implemented in SCAPS-1D software requires comprehensive material parameters for each layer of the device structure. All material properties and parameters utilized in this study are derived from established literature [8,10,32–39]. The simulation parameters are systematically organized in Tables 1–4, encompassing fundamental material properties of the Sb<sub>2</sub>Se<sub>3</sub> device, interface defect characteristics, HTL material specifications, and electrode parameters. Key simulation parameters include electron and hole capture cross-sections for both bulk and interface defects ( $10^{-15}$  cm<sup>2</sup>), radiative recombination coefficient ( $10^{-8}$  cm/s), and carrier thermal velocities ( $10^7$  cm/s for both electrons and holes, as detailed in Table 3). All simulations were performed under standardized conditions of 300 K and AM 1.5 G illumination ( $100$  mW/cm<sup>2</sup>), with initial analyses conducted without considering series and shunt resistance effects.

**Table 1.** Materials parameters used in the simulation.

Parameter	ITO [32]	i-ZnO [33]	CdS [33]	Sb <sub>2</sub> Se <sub>3</sub> [33]
Thickness (μm)	0.3	0.05	0.07	1.5
E <sub>g</sub> (eV)	3.6	3.3	2.4	1.17
χ (eV)	4.1	4.45	4.2	4.3
ε <sub>r</sub>	10	9	10	19
N <sub>C</sub> (1 cm <sup>-3</sup> )	$2.2 \times 10^{18}$	$2.2 \times 10^{18}$	$2.2 \times 10^{18}$	$2.2 \times 10^{18}$
N <sub>V</sub> (1 cm <sup>-3</sup> )	$1.8 \times 10^{19}$	$1.8 \times 10^{19}$	$1.8 \times 10^{19}$	$1.8 \times 10^{19}$
v <sub>th,e</sub> (cm/s)	$10^7$	$10^7$	$10^7$	$10^7$
v <sub>th,h</sub> (cm/s)	$10^7$	$10^7$	$10^7$	$10^7$

**Table 1.** Cont.

Parameter	ITO [32]	i-ZnO [33]	CdS [33]	Sb <sub>2</sub> Se <sub>3</sub> [33]
$\mu_e$ (cm <sup>2</sup> (V S) <sup>-1</sup> )	75	100	100	15
$\mu_h$ (cm <sup>2</sup> (V S) <sup>-1</sup> )	50	25	25	42
Donor density, $N_D$ (1/cm <sup>3</sup> )	10 <sup>19</sup>	10 <sup>18</sup>	10 <sup>17</sup>	0
Acceptor density, $N_A$ (1 cm <sup>-3</sup> )	0	10 <sup>18</sup>	10 <sup>2</sup>	10 <sup>16</sup>
Defect type		Acceptor	Donor	Neutral
Reference		Above E <sub>V</sub>	Above E <sub>V</sub>	Above E <sub>V</sub>
E <sub>t</sub> (eV)		0.6	0.6	0.6
$N_t$ (1 cm <sup>-3</sup> )		10 <sup>10</sup>	10 <sup>15</sup>	10 <sup>12</sup>

$\chi$ : electron affinity,  $\epsilon_r$ : dielectric permittivity (relative), N: effective density of states, C: conduction band, V: valence band,  $v_{th}$ : thermal velocity,  $\mu$ : mobility,  $N_A$ : shallow acceptor density,  $N_D$ : shallow donor density, E<sub>t</sub>: trap position,  $N_t$ : trap density.

**Table 2.** Interface defect simulation parameters used in the simulation.

Interface	i-ZnO/CdS [33]	CdS/Sb <sub>2</sub> Se <sub>3</sub> [33]	Sb <sub>2</sub> Se <sub>3</sub> /HTL [34]
Defect type	Neutral	Neutral	Neutral
$\sigma_e$ (cm <sup>2</sup> )	4 × 10 <sup>-18</sup>	1 × 10 <sup>-19</sup>	1 × 10 <sup>-19</sup>
$\sigma_h$ (cm <sup>2</sup> )	4 × 10 <sup>-18</sup>	1 × 10 <sup>-19</sup>	1 × 10 <sup>-19</sup>
$N_t$ (1 cm <sup>-2</sup> )	10 <sup>10</sup>	2.8 × 10 <sup>10</sup>	10 <sup>12</sup>

$\sigma$ : capture cross-section,  $N_t$ : trap density.

**Table 3.** Simulation parameters of HTL materials used in the simulation.

Parameter	CZ-TA [17]	Spiro [17]	CZTS [11]	Cu <sub>2</sub> O [35]	CuO [35]	CuI [35]	CuSCN [36]	NiO <sub>x</sub> [36]
Thickness (μm)	0.05	0.05	0.05	0.05	0.05	0.05	0.05	0.05
E <sub>g</sub> (eV)	3.10	2.91	1.4	2.17	1.51	3.1	3.4	3.8
$\chi$ (eV)	2.2	2.2	4.1	3.2	4.07	2.1	1.9	1.8
$\epsilon_r$	3	3	9	7.11	18.1	6.5	10.0	11.75
$N_C$ (cm <sup>-3</sup> )	8 × 10 <sup>17</sup>	8 × 10 <sup>17</sup>	2.2 × 10 <sup>18</sup>	2.02 × 10 <sup>17</sup>	2.2 × 10 <sup>19</sup>	2.8 × 10 <sup>19</sup>	2.2 × 10 <sup>18</sup>	2 × 10 <sup>18</sup>
$N_V$ (cm <sup>-3</sup> )	1.8 × 10 <sup>19</sup>	1.8 × 10 <sup>19</sup>	1.8 × 10 <sup>18</sup>	1.1 × 10 <sup>19</sup>	5.5 × 10 <sup>20</sup>	1.0 × 10 <sup>19</sup>	1.8 × 10 <sup>18</sup>	2 × 10 <sup>18</sup>
$\mu_e$ (cm <sup>2</sup> (VS) <sup>-1</sup> )	1.65 × 10 <sup>-4</sup>	6.17 × 10 <sup>-5</sup>	100	200	10	100	100	8
$\mu_h$ (cm <sup>2</sup> (VS) <sup>-1</sup> )	1.65 × 10 <sup>-4</sup>	6.17 × 10 <sup>-5</sup>	12.5	80	0.1	43.9	25	81.10
$N_D$ (1 cm <sup>-3</sup> )	0	0	0	0	0	0	0	0
$N_A$ (1 cm <sup>-3</sup> )	10 <sup>19</sup>	10 <sup>19</sup>	10 <sup>19</sup>	10 <sup>19</sup>	10 <sup>19</sup>	10 <sup>19</sup>	10 <sup>19</sup>	10 <sup>19</sup>

**Table 4.** Simulation parameters of contact materials used in the simulation.

Contacts	Al [37]	Mo [38]	FTO [39]
$W_f$	4.28	5.0	4.4
$S_e$	10 <sup>7</sup>	10 <sup>5</sup>	10 <sup>7</sup>
$S_h$	10 <sup>5</sup>	10 <sup>7</sup>	10 <sup>5</sup>
Reflection	No	No	No

$W_f$ : work function, S: surface recombination velocity.

### 3. Results and Discussion

#### 3.1. Comparison of Substrate and Superstrate Configurations

This investigation presents a systematic comparison of substrate and superstrate architectures in  $\text{Sb}_2\text{Se}_3$  solar cells. The substrate configuration implements a  $\text{Mo}/\text{Sb}_2\text{Se}_3/\text{CdS}/\text{i-ZnO}/\text{ITO}/\text{Al}$  structure (Figure 1a), whereas the superstrate variant employs a  $\text{FTO}/\text{CdS}/\text{Sb}_2\text{Se}_3/\text{Al}$  architecture (Figure 1b). Energy band alignments for both configurations are depicted in Figure 2. To ensure comparative validity, material layers and metal electrodes remained consistent, with contact parameters specified in Table 4. Utilizing parameters detailed in Tables 1 and 2, we obtained current–voltage characteristics and external quantum efficiency (EQE) curves through numerical simulation (Figure 3), with performance metrics compiled in Table 5.

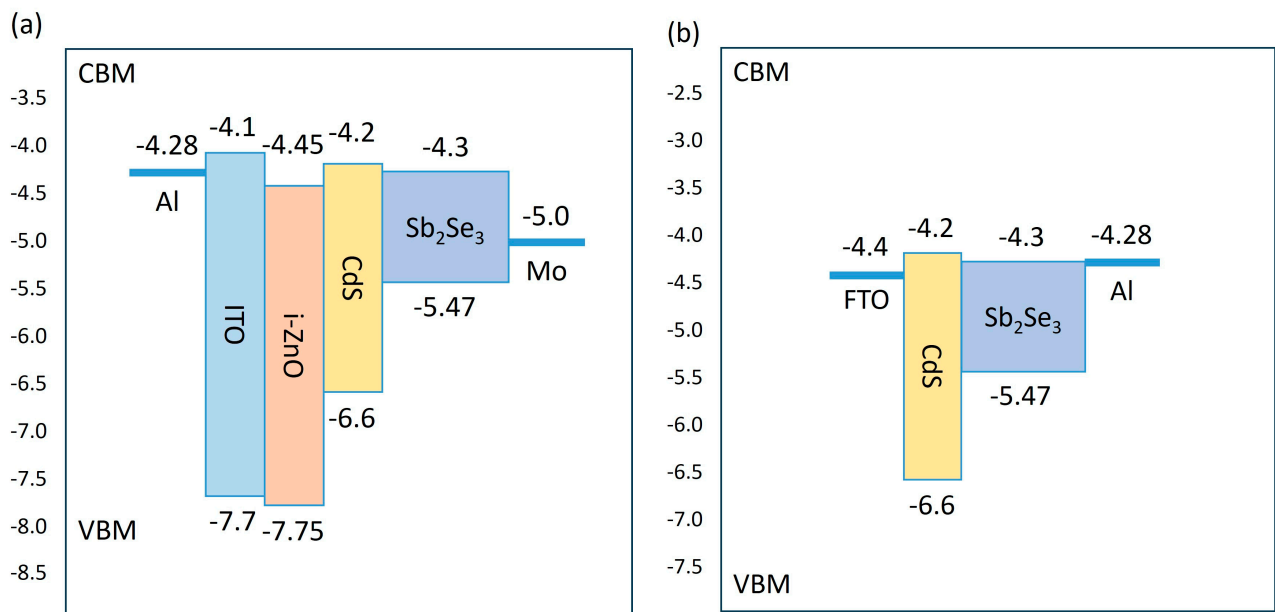


**Figure 2.** Energy band diagrams of different device configurations: (a) substrate and (b) superstrate structures.

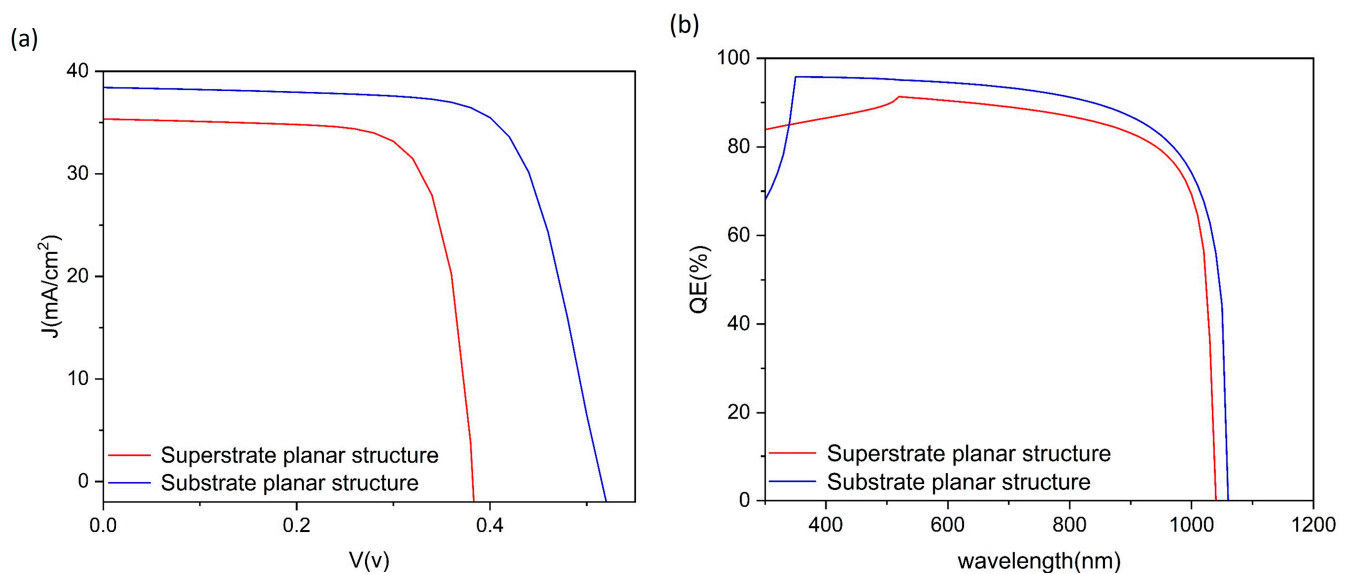


**Figure 3.** Performance characteristics of different device configurations: (a) current–voltage curves and (b) external quantum efficiency spectra.

**Table 5.** Device performance parameters for different configuration structures.

	$V_{OC}$ (V)	$J_{SC}$ (mA/cm <sup>2</sup> )	FF (%)	PCE (%)
Substrate	0.52	38.42	71.88	14.23
Superstrate	0.38	35.34	74.62	10.09
Superstrate with Au ( $W_f = 5.1$ )	0.52	35.66	75.21	13.83

Energy band structure analysis (Figure 2) reveals that the primary differentiation between configurations manifests in the electrode/absorber interface characteristics. The substrate configuration exhibits favorable energetics, with minimal energy-level difference between the Mo electrode (work function 4.9 eV) and Sb<sub>2</sub>Se<sub>3</sub> valence band (5.5 eV), enabling formation of a quasi-ohmic contact. This advantageous band alignment substantially reduces interfacial charge transfer resistance and minimizes non-radiative recombination at interface states. Conversely, the superstrate configuration's Al electrode, characterized by a lower work function (4.28 eV), generates a significant Schottky barrier (approximately 1.22 eV), hindering efficient photogenerated hole collection. Substitution of Al with Au (work function 5.1 eV) as the back contact reduces barrier height to approximately 0.4 eV, substantially improving interfacial characteristics. This enhancement manifests in device parameters (Table 5), elevating both the fill factor (FF) and open-circuit voltage (Voc) through reduced interface recombination.

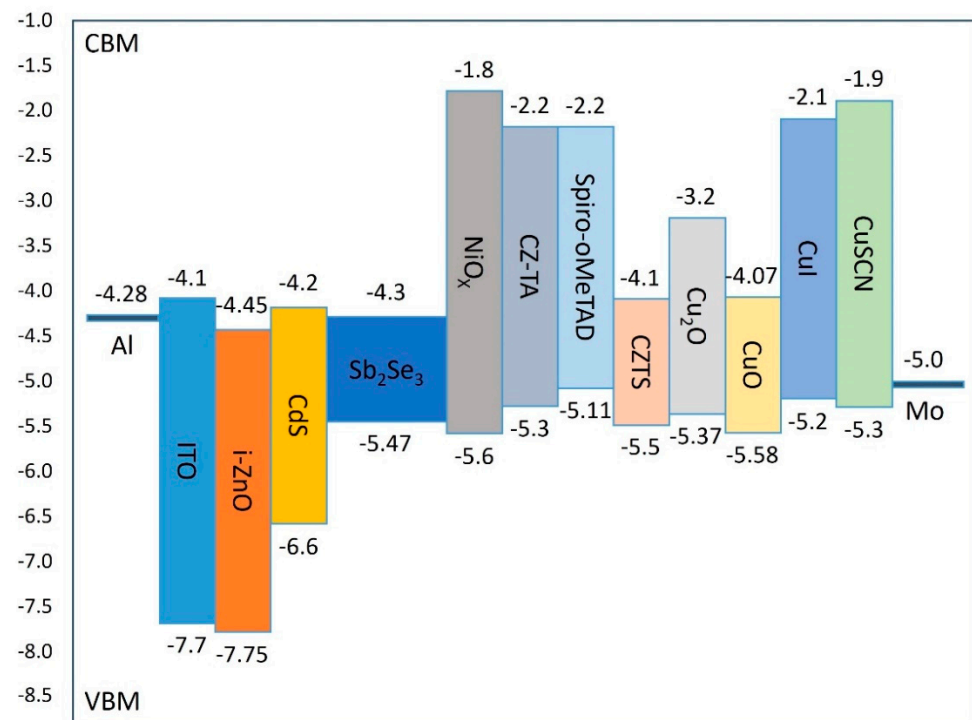
Current–voltage analysis (Figure 3a) demonstrates the substrate configuration's superior performance, achieving higher open-circuit voltage (0.52 V) and short-circuit current density (38.42 mA/cm<sup>2</sup>) compared with the superstrate design ( $V_{oc} = 0.38$  V,  $J_{sc} = 35.34$  mA/cm<sup>2</sup>). This performance enhancement primarily originates from the quasi-ohmic contact at the Mo/Sb<sub>2</sub>Se<sub>3</sub> interface, where optimal band alignment minimizes carrier injection/extraction barriers and voltage losses. EQE measurements (Figure 3b) further validate this advantage, with the substrate configuration exhibiting enhanced photoresponse across 400–1000 nm, particularly maintaining high quantum efficiency in the long-wavelength region (>800 nm). These characteristics indicate superior minority carrier collection efficiency and reduced bulk recombination. Despite a slightly lower fill factor in the substrate configuration (71.88% vs. 74.62%), potential exists for enhancement through interface engineering.

Significantly, implementation of Au electrodes in the superstrate configuration elevates performance (PCE = 13.83%) near that of the substrate configuration (PCE = 14.23%), confirming the critical role of electrode/absorber interface band alignment. Based on comprehensive evaluation of performance metrics, process compatibility, and interface stability, we selected the substrate configuration for subsequent optimization studies. This architecture demonstrates both superior photovoltaic conversion efficiency potential and clear pathways for further performance enhancement in Sb<sub>2</sub>Se<sub>3</sub> solar cells.

### 3.2. Comparison of Different HTL Materials

This investigation examines the performance characteristics of various HTL materials, with simulation parameters documented in Table 3. Figure 4 illustrates the energy band diagrams of different HTL materials within the complete device structure. Two critical band alignment requirements govern HTL material selection: First, the valence-band maximum (VBM) of the HTL must be positioned appropriately relative to both the back contact work function and the Sb<sub>2</sub>Se<sub>3</sub> VBM to facilitate efficient hole transfer. As is evident from the band diagrams, the VBMs of NiOx, CuO, and CZTS lie slightly below that of the Sb<sub>2</sub>Se<sub>3</sub> absorber layer, creating potential barriers that impede effective hole transport. Second, the conduction band minimum (CBM) of the HTL must exceed that of Sb<sub>2</sub>Se<sub>3</sub> to prevent electron backflow. Although CuO and CZTS exhibit CBM levels marginally higher than the Sb<sub>2</sub>Se<sub>3</sub> absorber layer, their relatively small energy offsets with the buffer layer results in inadequate electron blocking, failing to effectively prevent electron drift towards the back contact and increasing carrier recombination probability.





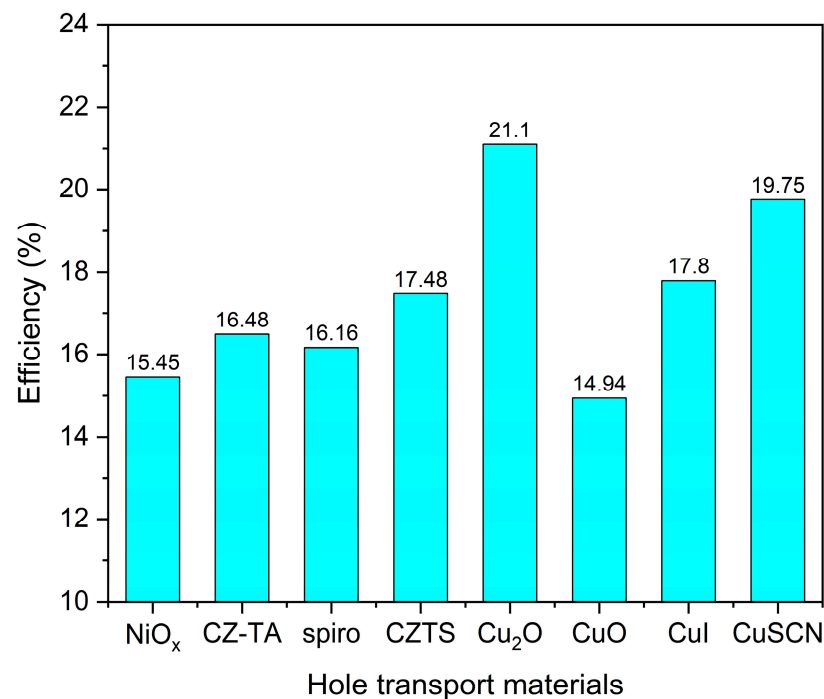
**Figure 4.** Energy band diagrams of various HTL materials in the device structure.

Table 6 presents the valence-band offset (VBO) values between each HTL and the  $\text{Sb}_2\text{Se}_3$  absorber layer, calculated using the modified Equation (2). These VBO values significantly impact device performance: positive VBO values (such as  $\text{Cu}_2\text{O}$  at 0.1 eV, CZ-TA at 0.17 eV, and Spiro at 0.36 eV) create appropriate energy barriers at the absorber/HTL interface, contributing to electron blocking functionality. Conversely, negative VBO values (such as  $\text{NiO}_x$  at  $-0.13$  eV and  $\text{CuO}$  at  $-0.11$  eV) form energy wells at the interface, increasing carrier recombination probability. Simulation results, as shown in Figure 5, demonstrate that  $\text{Cu}_2\text{O}$  achieves the highest PCE (21.1%) as an HTL material due to its moderate positive VBO (0.1 eV), which provides electron blocking capabilities without excessively hindering hole transport. This optimal performance is further enhanced by  $\text{Cu}_2\text{O}$ 's superior carrier mobility characteristics.

**Table 6.** Calculated VBO values for different HTL materials.

HTL	$\text{NiO}_x$	CZ-TA	Spiro	CZTS	$\text{Cu}_2\text{O}$	$\text{CuO}$	$\text{CuI}$	$\text{CuSCN}$
VBO	$-0.13$	0.17	0.36	$-0.03$	0.1	$-0.11$	0.27	0.17

Analysis reveals several key structure–property relationships. Materials with moderate positive VBO values (0.1–0.2 eV) exhibit superior performance by achieving an optimal balance between electron blocking and hole transport.  $\text{Cu}_2\text{O}$ 's exceptional performance stems from its optimal band alignment and high carrier mobility (approximately  $10^{-2} \text{ cm}^2/\text{V}\cdot\text{s}$ ), facilitating efficient hole extraction. In contrast, materials with larger positive VBO values, such as Spiro (0.36 eV), generate excessive barriers for hole transport despite effective electron blocking. The negative VBO values observed in  $\text{NiO}_x$  and  $\text{CuO}$  not only fail to block electrons effectively but also create potential wells that trap holes, leading to increased interface recombination and reduced device efficiency.



**Figure 5.** PCE comparison of different HTL materials.

### 3.3. Effects of Cu<sub>2</sub>O Thickness and Shallow Acceptor Density on Device Performance

The influence of Cu<sub>2</sub>O thickness on device performance is characterized in Figure 6, with thickness variations examined from 0.01  $\mu\text{m}$  to 0.1  $\mu\text{m}$ . Throughout this range, the open-circuit voltage ( $V_{oc}$ ) maintains relative stability at approximately 0.68 V, attributable to ideal solar cell behavior where light penetration and minority carrier collection remain optimal. Increasing Cu<sub>2</sub>O thickness extends the optical path length through the HTL, enhancing photon absorption and carrier generation, consequently improving short-circuit current density ( $J_{sc}$ ). An optimized HTL thickness facilitates balanced electron and hole transport rates, minimizing interface charge accumulation and enhancing the fill factor. However, excessive Cu<sub>2</sub>O layer thickness leads to carrier recombination before electrode collection, reducing carrier collection efficiency, conductivity,  $J_{sc}$ , fill factor, and overall performance. Simulation results establish optimal photoelectric conversion efficiency of 21.43% at 0.06  $\mu\text{m}$  thickness. Shallow acceptor density characterizes the concentration of hole acceptors proximate to the conduction band edge in semiconductors. These acceptors, introduced through impurity atoms or intrinsic defects, exhibit energy levels within 0.1 eV of the conduction band edge, effectively capturing photo-excited holes and reducing recombination losses, thereby enhancing photoelectric conversion efficiency.

Figure 7 illustrates the correlation between Cu<sub>2</sub>O HTL shallow acceptor density and device performance. Performance enhancement becomes significant above  $10^{16} \text{ cm}^{-3}$ , corresponding to the absorption layer's shallow acceptor density. Exceeding this threshold creates an effective back potential barrier, with increased shallow acceptor density improving conductivity,  $J_{sc}$ , fill factor, and overall efficiency while reducing series resistance. However, continued density increases shift the Fermi level toward the valence band. At excessive densities, the Fermi level enters the valence band, creating high hole concentrations and transforming the semiconductor into a strong p-type conductor, potentially causing simulation convergence failures.



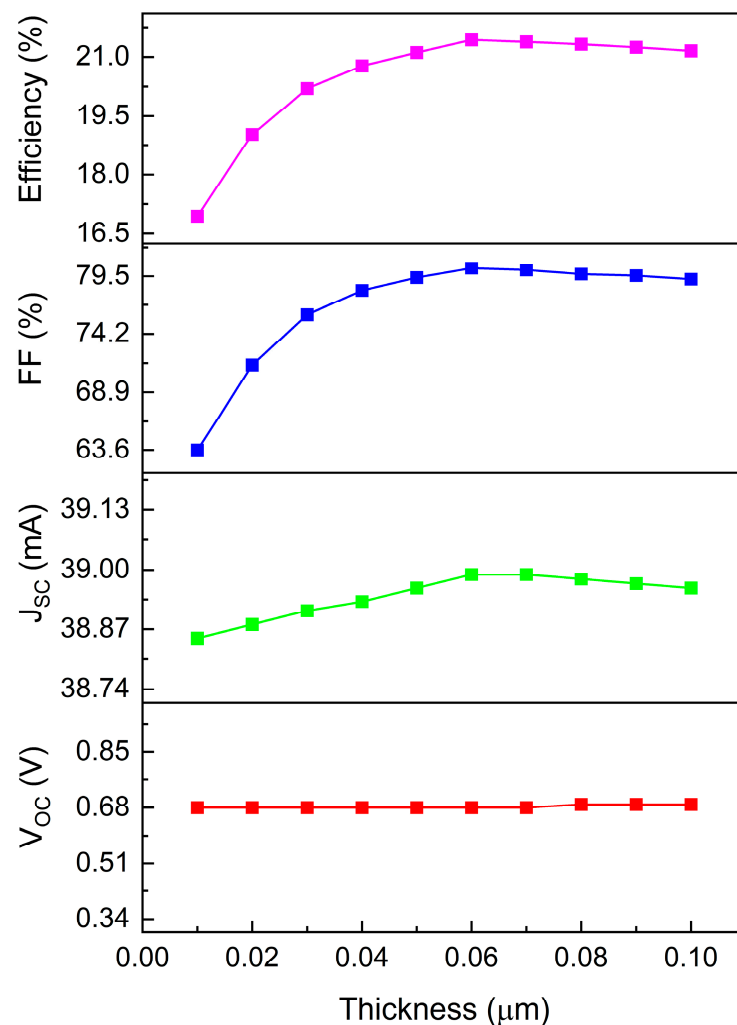


**Figure 6.** Relationship between  $\text{Cu}_2\text{O}$  HTL thickness and device performance.

Figure 8 presents a comprehensive visualization of device efficiency as a function of both  $\text{Cu}_2\text{O}$  HTL thickness and shallow acceptor density, displayed through a color-mapped surface plot. In the low acceptor density region ( $10^{12}$ – $10^{15}$   $\text{cm}^{-3}$ ), device efficiency remains relatively low, particularly when combined with HTL thicknesses below  $0.04$   $\mu\text{m}$ . The plot reveals a critical transition around  $10^{16}$   $\text{cm}^{-3}$  acceptor density, above which device performance significantly improves. Notably, devices with HTL thickness near  $0.06$   $\mu\text{m}$  demonstrate optimal performance and exhibit greater stability across acceptor density variations, suggesting a favorable processing window for device fabrication. The highest efficiency region, indicated by the red area in the plot, occurs at the combination of  $0.06$   $\mu\text{m}$  HTL thickness and acceptor densities above  $10^{18}$   $\text{cm}^{-3}$ . Under these optimal conditions ( $0.06$   $\mu\text{m}$  thickness,  $10^{19}$   $\text{cm}^{-3}$  acceptor density), the device achieves peak performance parameters:  $V_{oc} = 0.69$  V,  $J_{sc} = 39.11$   $\text{mA}/\text{cm}^2$ ,  $\text{FF} = 80.88\%$ , and overall efficiency of  $21.68\%$ . This efficiency enhancement can be attributed to improved carrier transport and reduced interface recombination at higher acceptor densities, while the optimal thickness ensures effective light absorption without excessive carrier transport losses.

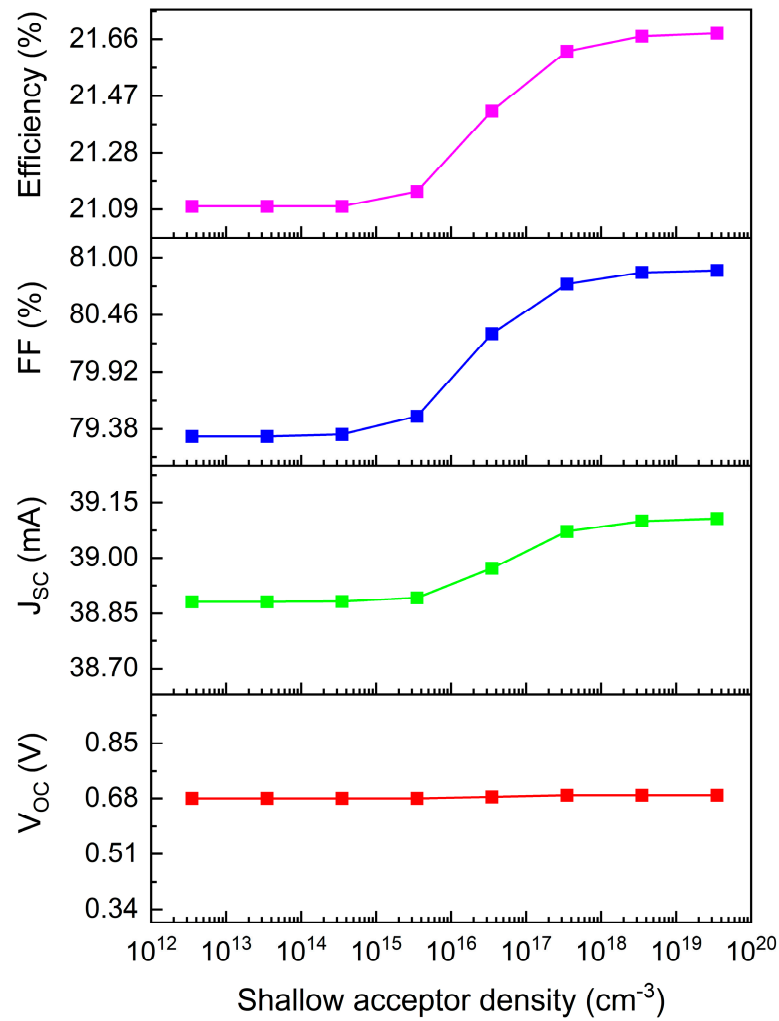


Figure 7. Relationship between  $\text{Cu}_2\text{O}$  HTL shallow acceptor density and device performance.

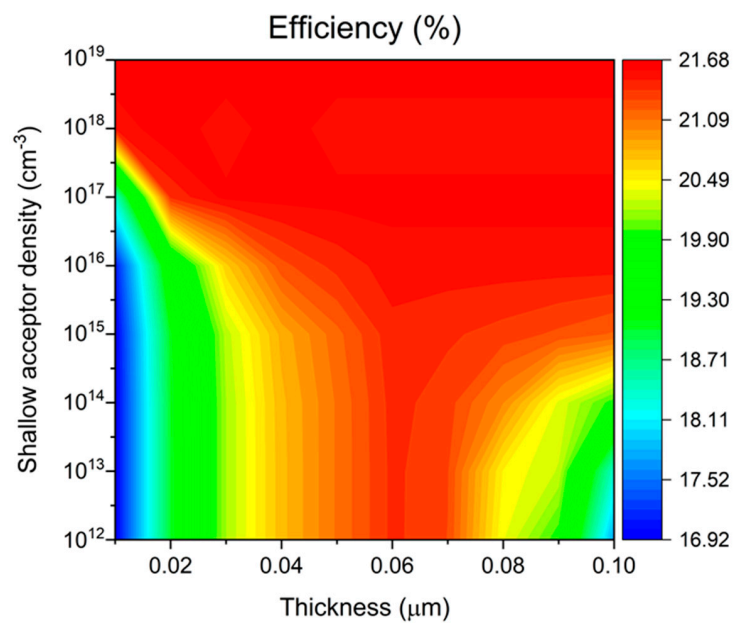
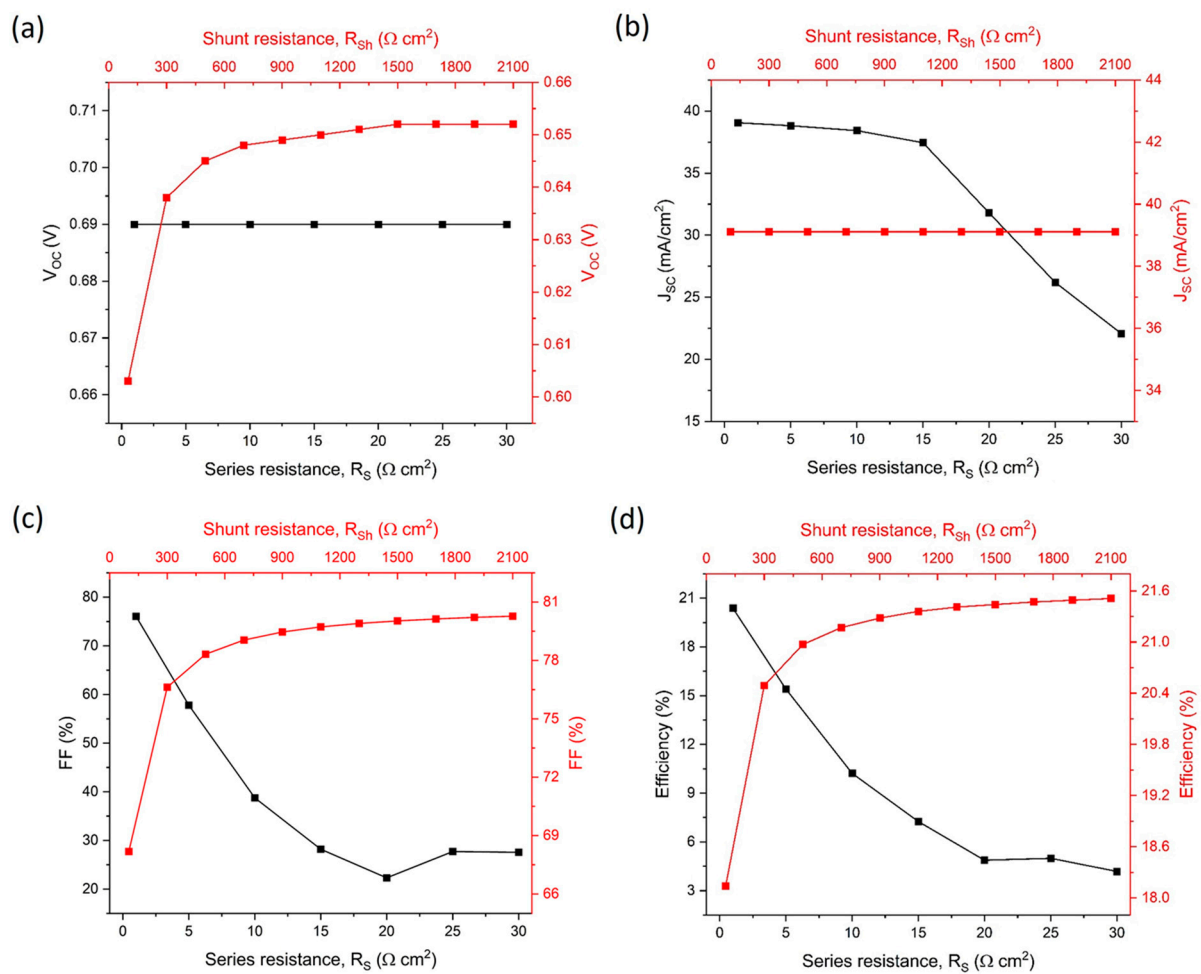


Figure 8. Effect of shallow acceptor density on  $\text{Sb}_2\text{Se}_3$  solar-cell efficiency at different  $\text{Cu}_2\text{O}$  HTL thicknesses.

### 3.4. Effects of Series and Shunt Resistance on Device Performance

To investigate the influence of series resistance ( $R_s$ ) and shunt resistance ( $R_{sh}$ ), we maintained all other parameters at their optimized values. The impact of these resistances on solar-cell performance is illustrated in Figure 9, with  $R_s$  varying from 1–30  $\Omega\text{-cm}^2$  and  $R_{sh}$  from 100–2100  $\Omega\text{-cm}^2$ . Both parameters demonstrate significant influence on overall device efficiency. Figure 9a,b reveal distinct relationships between resistance parameters and device characteristics: the open-circuit voltage ( $V_{oc}$ ) exhibits slight enhancement with increasing  $R_{sh}$  while remaining independent of  $R_s$  variations. Conversely, short-circuit current density ( $J_{sc}$ ) shows strong  $R_s$  dependence while maintaining relative stability with  $R_{sh}$  variations. This behavior aligns with Ohm's law ( $V = IR$ ): during open-circuit conditions, current absence through  $R_s$  results in zero voltage drop, rendering  $V_{oc}$  independent of  $R_s$  magnitude. Under short-circuit conditions, the external circuit resistance becomes negligible compared to  $R_{sh}$ , directing photogenerated current predominantly through the external circuit. Analysis of Figure 9c,d reveals substantial performance dependencies: increasing  $R_s$  severely degrades the fill factor (FF) from 76.05% to 27.55%, with corresponding efficiency reduction from 20.38% to 4.18%. In contrast, enhanced  $R_{sh}$  improves device performance, elevating FF from 68.18% to 80.27% and efficiency from 18.14% to 21.51%. These findings establish optimal performance parameters for  $\text{Sb}_2\text{Se}_3$  solar cells:  $R_s$  should be minimized to 0–5  $\Omega\text{-cm}^2$ , while  $R_{sh}$  should exceed 2000  $\Omega\text{-cm}^2$ .



**Figure 9.** Numerical analysis of series and parallel resistance on device performance. (a) Open-circuit voltage ( $V_{oc}$ ) variation, (b) Short-circuit current density ( $J_{sc}$ ) response, (c) Fill Factor (FF) dependence, and (d) Device efficiency changes with respect to series and parallel resistance.

#### 4. Conclusions

This study utilized SCAPS-1D software to conduct numerical simulation and performance optimization of  $\text{Sb}_2\text{Se}_3$  thin-film solar cells. The investigation focused on key parameters including solar-cell device structures (substrate and superstrate configurations), various hole-transport layer (HTL) materials ( $\text{NiO}_x$ , CZTS,  $\text{Cu}_2\text{O}$ ,  $\text{CuO}$ ,  $\text{CuI}$ ,  $\text{CuSCN}$ , CZTA, and Spiro-OMeTAD), their thicknesses, shallow acceptor densities, and the effects of series and shunt resistances. Through systematic analysis, the substrate configuration with Mo back contact demonstrated superior performance compared to the superstrate configuration. Among the various HTL materials investigated,  $\text{Cu}_2\text{O}$  exhibited the highest photoelectric efficiency due to its smallest VBO value. The study revealed that HTL thickness control is more critical than carrier concentration control, with  $\text{Cu}_2\text{O}$  HTL achieving optimal photoelectric conversion efficiency at 0.06  $\mu\text{m}$  thickness. This configuration provided a wide process window, as the efficiency showed relatively low sensitivity to changes in shallow acceptor density. For achieving high-efficiency  $\text{Sb}_2\text{Se}_3$  solar cells, the research established that series resistance should be reduced (to 0–5  $\Omega\text{-cm}^2$ ) and shunt resistance increased (to above 2000  $\Omega\text{-cm}^2$ ), which significantly improved both the fill factor and photoelectric conversion efficiency. Under optimized conditions utilizing the Mo/ $\text{Cu}_2\text{O}$ (0.06  $\mu\text{m}$ )/ $\text{Sb}_2\text{Se}_3$ /CdS/i-ZnO/ITO/Al structure, the device showed significantly improved photoelectric conversion efficiency from 14.23% (conventional cells without HTL) to a maximum of 21.68% with the optimized  $\text{Cu}_2\text{O}$  HTL.

Looking forward, several promising research directions emerge from this work. Further interface engineering studies could focus on novel buffer layer materials and surface passivation techniques to minimize recombination losses. Material development efforts should explore new HTL alternatives with enhanced band alignment and carrier transport properties, while also considering stability and cost-effectiveness. Device architecture optimization could investigate tandem configurations and alternative contact materials. Additionally, practical implementation aspects such as scalable fabrication processes, long-term stability, and cost-benefit analyses of different materials and structures warrant investigation. These future directions are aimed at bridging the gap between simulated theoretical performance and practical device implementation, ultimately advancing the development of high-efficiency  $\text{Sb}_2\text{Se}_3$  solar cells for real-world applications.

**Author Contributions:** Conceptualization, Y.-C.L.; Data curation, C.-K.L.; Writing—original draft, C.-K.L.; Writing—review & editing, Y.-C.L.; Supervision, Y.-C.L. All authors have read and agreed to the published version of the manuscript.

**Funding:** This research was funded by National Science and Technology Council under grant number 113-2221-E-018-001.

**Institutional Review Board Statement:** Not applicable.

**Informed Consent Statement:** Not applicable.

**Data Availability Statement:** The original contributions presented in this study are included in the article. Further inquiries can be directed to the corresponding author.

**Acknowledgments:** The authors wish to thank the developers of SCAPS at the University of Gent for making their software package publicly available free of charge. The authors also like to acknowledge the financial support of the National Science and Technology Council under grant number 113-2221-E-018-001.

**Conflicts of Interest:** The authors declare no conflict of interest.

#### References

1. Duan, M.; Zhang, X.; Chen, Y.; Wang, L.; Yang, J.; Liu, F.; Yang, P.; Tang, Z.; Zhou, W.; Chen, S.  $\text{Sb}_2\text{Se}_3$  Thin-film solar cells exceeding 10% power conversion efficiency enabled by injection vapor deposition technology. *Adv. Mater.* **2022**, *34*, 2202969. [[CrossRef](#)] [[PubMed](#)]
2. Zhou, Y.C.; Wang, L.; Chen, S.; Mahadik, S.K.; Liu, A.; Zhu, C.; Zhang, W.; Yang, H.; Gao, M.; Chen, S. High-efficiency flexible  $\text{Sb}_2\text{Se}_3$  solar cells by back interface and absorber bulk deep-level trap engineering. *ACS Energy Lett.* **2022**, *7*, 2095–2102.

3. Zeng, Y.; Xie, S.Y.; Chen, C.H.; Fan, J.D.; Yang, R.X. A review of  $\text{Sb}_2\text{Se}_3$  photovoltaic absorber materials and thin-film solar cells. *Sol. Energy Mater. Sol. Cells* **2016**, *151*, 57–70.
4. Liu, X.; Chen, J.; Yang, M.; Zhou, Y.; Chen, S.; Liu, Z.; Tang, J. Efficient  $\text{Sb}_2\text{Se}_3$  solar cells with Sb and Ge co-doping. *J. Mater. Chem. A* **2022**, *10*, 10060–10068.
5. Zhang, X.; Li, Y.; Sun, J.; Liu, H.; Liu, X.; Zhou, Y. Efficient  $\text{Sb}_2\text{Se}_3$  solar cells with defect engineering and surface passivation. *ACS Energy Lett.* **2023**, *8*, 47–55.
6. Chen, X.; Sun, L.; Li, Y.; Zhang, H.; Wang, X.; Tang, J. Solvent-assisted hydrothermal deposition approach for highly-efficient  $\text{Sb}_2(\text{S,Se})_3$  thin-film solar cells. *Adv. Energy Mater.* **2023**, *23*, 2300391. [[CrossRef](#)]
7. Wang, X.; Li, Y.; Liu, Z.; Yang, W.; Chen, S. Efficient  $\text{Sb}_2\text{Se}_3$  solar cells with a new hole transport layer. *Nano Energy* **2022**, *87*, 105803.
8. Guo, L.; Vijayaraghavan, S.N.; Duan, X.; Menon, H.G.; Wall, J.; Kong, L.; Yan, F. Stable and efficient  $\text{Sb}_2\text{Se}_3$  solar cells with solution-processed  $\text{NiO}_x$  hole-transport layer. *Sol. Energy* **2021**, *218*, 525–531. [[CrossRef](#)]
9. Li, P.; Yuan, X.; Feng, M.; Ran, F.; Zhang, D.; Chen, S. Fabrication of  $\text{TiO}_x/\text{Sb}_2\text{Se}_3/\text{p-NiO}_x$  photocathode for efficient photoelectrochemical water reduction. *Appl. Phys. Lett.* **2021**, *119*, 100445.
10. Mu, F.; Liu, Z.; Zi, W.; Cao, Y.; Lu, X.; Li, Y.; Cheng, N. CZTS nanoparticles as an effective hole-transport layer for  $\text{Sb}_2\text{Se}_3$  thin-film solar cells. *Sol. Energy* **2021**, *226*, 154–160. [[CrossRef](#)]
11. Maurya, K.K.; Singh, V.N.  $\text{Sb}_2\text{Se}_3/\text{CZTS}$  dual absorber layer based solar cell with 36.32% efficiency: A numerical simulation. *J. Sci. Adv. Mater. Dev.* **2022**, *7*, 100445.
12. Li, Z.Q.; Ni, M.; Feng, X.D. Simulation of the  $\text{Sb}_2\text{Se}_3$  solar cell with a hole transport layer. *Mater. Res. Express* **2020**, *7*, 016416. [[CrossRef](#)]
13. Sultana, B.; Islam, A.S.; Haque, M.D.; Kuddus, A.  $\text{Cu}_2\text{O}$ -Enhanced Back Surface Field Empowers Selenium-Based  $\text{TiO}_2/\text{Sb}_2\text{Se}_3$  Thin Film Solar Cells to Achieve Efficiency over 32%. *Appl. Sol. Energy* **2023**, *59*, 836–850. [[CrossRef](#)]
14. Lee, S.; McInerney, M.F. Optimization of bifacial Ge-incorporated  $\text{Sb}_2\text{Se}_3$  thin-film solar cells by modeling  $\text{Cu}_2\text{O}$  back buffer layer. *Sol. Energy Mater. Sol. Cells* **2023**, *257*, 112399. [[CrossRef](#)]
15. Christians, J.A.; Kamat, P.V. Trap and transfer. Two-step hole injection across the  $\text{Sb}_2\text{S}_3/\text{CuSCN}$  interface in solid-state solar cells. *ACS Nano* **2013**, *7*, 7967–7974. [[CrossRef](#)]
16. Li, K.; Wang, S.; Chen, C.; Kondrotas, R.; Hu, M.; Lu, S.; Tang, J. 7.5% n-i-p  $\text{Sb}_2\text{Se}_3$  solar cells with  $\text{CuSCN}$  as a hole-transport layer. *J. Mater. Chem. A* **2019**, *7*, 9665–9672. [[CrossRef](#)]
17. Ngoupo, A.T.; Ouédraogo, S.; Zougmore, F.; Ndjaka, J.M.B. Numerical analysis of ultrathin  $\text{Sb}_2\text{Se}_3$ -based solar cells by SCAPS-1D numerical simulator device. *Chin. J. Phys.* **2021**, *70*, 1–13. [[CrossRef](#)]
18. Li, D.B.; Yin, X.; Grice, C.R.; Guan, L.; Song, Z.; Wang, C.; Tang, J. Stable and efficient  $\text{CdS}/\text{Sb}_2\text{Se}_3$  solar cells prepared by scalable close space sublimation. *Nano Energy* **2018**, *49*, 346–353. [[CrossRef](#)]
19. Joy, A.; Abir, A.T.; Mondal, B.K.; Hossain, J. Numerical studies on a ternary  $\text{AgInTe}_2$  chalcopyrite thin film solar cell. *Heliyon* **2023**, *9*, e15876. [[CrossRef](#)]
20. Liu, L.; Zhang, S.L.; Wu, J.Y.; Wang, W.H.; Liu, W.; Wu, L.; Zhang, Y. Current improvement in substrate structured  $\text{Sb}_2\text{S}_3$  solar cells with  $\text{MoSe}_2$  interlayer. *Chin. Phys. B* **2020**, *29*, 058801. [[CrossRef](#)]
21. Ngoupo, A.T.; Ndjaka, J.M.B. Performance enhancement of  $\text{Sb}_2\text{Se}_3$ -based solar cell with hybrid buffer layer and  $\text{MoSe}_2$  as a hole transport material using simulator device. *Discov. Mech. Eng.* **2022**, *1*, 5. [[CrossRef](#)]
22. Guijarro, N.; Lutz, T.; Lana-Villarreal, T.; O'Mahony, F.; Gómez, R.; Haque, S.A. Toward antimony selenide sensitized solar cells: Efficient charge photogeneration at spiro-OMeTAD/ $\text{Sb}_2\text{Se}_3$ /metal oxide heterojunctions. *J. Phys. Chem. Lett.* **2012**, *3*, 1351–1356. [[CrossRef](#)] [[PubMed](#)]
23. Du, Q.; Shen, Z.; Chen, C.; Li, F.; Jin, M.; Li, H.; Wang, M. Spiro-OMeTAD:  $\text{Sb}_2\text{S}_3$  Hole Transport Layer with Triple Functions of Overcoming Lithium Salt Aggregation, Long-Term High Conductivity, and Defect Passivation for Perovskite Solar Cells. *Sol. RRL* **2021**, *5*, 2100622. [[CrossRef](#)]
24. Bera, A.; Mahapatra, A.D.; Mondal, S.; Basak, D.  $\text{Sb}_2\text{S}_3$ /Spiro-OMeTAD inorganic-organic hybrid p-n junction diode for high performance self-powered photodetector. *ACS Appl. Mater. Interfaces* **2016**, *8*, 34506–34512. [[CrossRef](#)]
25. Hernandez-Como, N.; Morales-Acevedo, A. Simulation of hetero-junction silicon solar cells with AMPS-1D. *Sol. Energy Mater. Sol. Cells* **2010**, *94*, 62–67. [[CrossRef](#)]
26. Hadjab, M.; Wagner, J.M.; Bouzid, F.; Boudour, S.; Larbi, A.H.; Bennacer, H.; Berrah, S. A numerical optimization study of  $\text{CdS}$  and  $\text{Mg}_{0.125}\text{Zn}_{0.875}\text{O}$  buffer layers in CIGS-based solar cells using wxAMPS-1D package. *Int. J. Model. Simul.* **2022**, *42*, 179–191. [[CrossRef](#)]
27. Smucker, J.; Gong, J. A comparative study on the band diagrams and efficiencies of silicon and perovskite solar cells using wxAMPS and AMPS-1D. *Sol. Energy* **2021**, *228*, 187–199. [[CrossRef](#)]
28. Al-Hattab, M.; Khenfouch, M.; Bajjou, O.; Chrafi, Y.; Rahmani, K. Numerical simulation of a new heterostructure CIGS/GaSe solar cell system using SCAPS-1D software. *Sol. Energy* **2021**, *227*, 13–22. [[CrossRef](#)]
29. Basak, A.; Singh, U.P. Numerical modelling and analysis of earth abundant  $\text{Sb}_2\text{S}_3$  and  $\text{Sb}_2\text{Se}_3$  based solar cells using SCAPS-1D. *Sol. Energy Mater. Sol. Cells* **2021**, *230*, 111184. [[CrossRef](#)]
30. Islam, M.S.; Sobayel, K.; Al-Kahtani, A.; Islam, M.A.; Muhammad, G.; Amin, N.; Akhtaruzzaman, M. Defect study and modelling of  $\text{SnX}_3$ -based perovskite solar cells with SCAPS-1D. *Nanomaterials* **2021**, *11*, 1218. [[CrossRef](#)]

31. Lovergine, N.; Cingolani, R.; Mancini, A.M.; Ferrara, M. Photoluminescence of CVD grown CdS epilayers on CdTe substrates. *J. Cryst. Growth* **1992**, *118*, 304–308. [[CrossRef](#)]
32. Srinivas, B.; Babujani, S.; Chandra, G.H.; Subbaiah, Y.P.V.; Gupta, M. Synthesis and characterization of Cu-sandwiched Sb<sub>2</sub>Se<sub>3</sub> thin films and numerical simulation of p-Sb<sub>2</sub>Se<sub>3</sub>/n-ZnSe heterojunction solar cell. *Opt. Mater.* **2023**, *135*, 113289. [[CrossRef](#)]
33. Moujoud, S.; Hartiti, B.; Touhtouh, S.; Belhora, F.; Hajjaji, A. Optimizing Sb<sub>2</sub>Se<sub>3</sub> thin-film solar cells: A comprehensive simulation study of multiple influential factors. *Optik* **2024**, *303*, 171723. [[CrossRef](#)]
34. Cao, Y.; Zhu, X.; Chen, H.; Zhang, X.; Zhou, J.; Hu, Z.; Pang, J. Towards high efficiency inverted Sb<sub>2</sub>Se<sub>3</sub> thin film solar cells. *Sol. Energy Mater. Sol. Cells* **2019**, *200*, 109945. [[CrossRef](#)]
35. Ranjan, R.; Anand, N.; Tripathi, M.N.; Srivastava, N.; Sharma, A.K.; Yoshimura, M.; Chang, L.; Tiwari, R.N. SCAPS study on the effect of various hole transport layer on highly efficient 31.86% eco-friendly CZTS based solar cell. *Sci. Rep.* **2023**, *13*, 18411. [[CrossRef](#)]
36. Abdur, R.; Choudhury, S.; Bashar, M.S.; Mossain, M.R.; Quddus, M.S.; Akhtar, U.S.; Shaikh, M.A.A.; Hossain, M.; Jamal, M.S. Enhancing perovskite solar cell performance: Investigating the impact of post-annealing on the optoelectrical and structural properties of RF-sputtered NiO films via SCAPS-1D device modeling. *Sol. Energy* **2024**, *271*, 112443. [[CrossRef](#)]
37. Karade, V.C.; Jang, J.S.; Kumbhar, D.; Rao, M.; Pawar, P.S.; Kim, S.; Gour, K.S.; Park, J.; Heo, J.; Dongale, T.D.; et al. Combating open circuit voltage loss in Sb<sub>2</sub>Se<sub>3</sub> solar cell with an application of SnS as a back surface field layer. *Sol. Energy* **2022**, *233*, 435–445. [[CrossRef](#)]
38. Mamta Maurya, K.K.; Singh, V.N. Sb<sub>2</sub>Se<sub>3</sub> as an HTL for Mo/Sb<sub>2</sub>Se<sub>3</sub>/Cs<sub>2</sub>TiF<sub>6</sub>/TiO<sub>2</sub> solar structure: Performance evaluation with SCAPS-1D. *Heliyon* **2022**, *8*, e10925. [[CrossRef](#)]
39. Azhakanantham, D.; Selvamani, M.; Kim, T.G.; Contreras, D.; Kesavan, A.V. Exploring novel HTL suitable for Eco-friendly and high performance FASnI<sub>3</sub> photovoltaics. *Mater. Sci. Eng. B* **2022**, *284*, 115789. [[CrossRef](#)]

**Disclaimer/Publisher's Note:** The statements, opinions and data contained in all publications are solely those of the individual author(s) and contributor(s) and not of MDPI and/or the editor(s). MDPI and/or the editor(s) disclaim responsibility for any injury to people or property resulting from any ideas, methods, instructions or products referred to in the content.